



## Tuning antimicrobial properties of biomimetic nanopatterned surfaces

Journal:	<i>Nanoscale</i>
Manuscript ID	NR-ART-01-2018-000439.R1
Article Type:	Paper
Date Submitted by the Author:	03-Mar-2018
Complete List of Authors:	Michalska, Martyna; Argonne National Laboratory, Biosciences Division Gambacorta, Francesca; Argonne National Laboratory, Biosciences Division Divan, Ralu; Argonne National Laboratory, Center for Nanoscale Materials Aranson, Igor; Argonne National Laboratory, Materials Science Division; Pennsylvania State University, Department of Biomedical Engineering Sokolov, Andrey; Argonne National Laboratory, Materials Science Division Noirot, Philippe; Argonne National Laboratory, Biosciences Division Laible, Philip; Argonne National Laboratory, Biosciences Division



Journal Name

ARTICLE

## Tuning antimicrobial properties of biomimetic nanopatterned surfaces

Received 00th January 20xx,  
Accepted 00th January 20xx

DOI: 10.1039/x0xx00000x

www.rsc.org/

Martyna Michalska,<sup>a</sup> Francesca Gambacorta,<sup>a</sup> Ralu Divan,<sup>b</sup> Igor S. Aranson,<sup>c,d</sup> Andrey Sokolov,<sup>c</sup> Philippe Noirots<sup>a</sup> & Philip D. Laible,<sup>\*a</sup>

Nature has amassed an impressive array of structures that afford protection from microbial colonization/infection when displayed on the exterior surfaces of organisms. Here, controlled variation of the features of mimetics derived from etched silicon allows for tuning and control of their antimicrobial efficacy. Materials with nanopillars up to 7  $\mu\text{m}$  in length are extremely effective against a wide range of microbial species and exceed the performance of natural surfaces; in contrast, materials with shorter/blunter nanopillars (< 2  $\mu\text{m}$ ) selectively killed specific species. Using a combination of microscopies, the mechanisms by which bacteria are killed are demonstrated, emphasizing the dependence upon pillar density and tip geometry. Additionally, real-time imaging reveals how cells are immobilized and killed rapidly. Generic or selective protection from microbial colonization could be conferred to surfaces [for, e.g., internal medicine, implants (joint, dental, and cosmetic), food preparation, and the agricultural industry] patterned with these materials as coatings.

### 1. Introduction

Novel materials are being used increasingly in medical applications. In parallel, there is a strong need for protecting the surfaces of these materials from colonization by microorganisms that can form biofilms and be directly harmful to patients<sup>1</sup> or indirectly impact treatment by, e.g., clogging pumps and tubes (biofouling) of medical equipment. Additionally, the emergence of multi-drug-resistant bacteria that cannot be eliminated by treatment with an antibiotic or cocktails thereof has prompted the search for novel strategies to prevent and/or effectively eliminate microbial colonization.<sup>2</sup> Recently, biomimetic surfaces with nanoscale topologies that exhibit antimicrobial properties have gained a lot of attention.<sup>3</sup> Such materials – including black silicon (bSi),<sup>4</sup> patterned titanium nanowires,<sup>5,6</sup> nanotextured polymers,<sup>7</sup> and silicon nanowire arrays<sup>8</sup> – contain nanopillars with dimensions and spacing similar to that of the waxy protrusions on plants and insect wings (e.g., cicada, dragonfly) that are responsible for keeping these surfaces free of microbes (anti-biofouling; reviewed by Nguyen *et al.*).<sup>9</sup> Among these nanotextured materials, bSi is extremely promising as it has proven to be biocompatible<sup>10</sup> and also exhibits bactericidal activity while

supporting growth and proliferation of much larger eukaryotic cells.<sup>11</sup>

Several methods can be employed to fabricate such nanotextured materials, including bSi.<sup>12–16</sup> Reactive-ion etching (RIE) is a scalable and cost-effective technique during which bSi topographical features can be modulated by varying process conditions such as gas composition and flow rate, temperature, etching time, pressure, DC self-bias voltage, and radio frequency power.<sup>17–21</sup>

To be used as an effective antimicrobial agent, bSi needs to act on bacterial cell envelopes, which naturally display a high diversity in chemical and mechanical properties.<sup>22</sup> The killing mechanism of bSi is proposed to be direct biomechanical penetration of cells by the sharp nanopillars.<sup>4</sup> This mode of action contrasts with what is believed to be occurring with natural nanotextured surfaces where nanopillars are thicker, blunt, dense and promote bacterial adhesion between multiple spikes. On the latter surfaces, the cell body becomes suspended between neighboring spikes, imposing stress on the outer membrane and cell wall, eventually reaching a stretching threshold that causes rupture, killing the organism.<sup>23</sup> Recently, another bactericidal mechanism for naturally occurring surfaces has been proposed where cells are disrupted as they attempt to move because of strong adhesion between bacteria and nanopillars.<sup>24</sup>

Regardless, nanotextured surface-mediated cell killing depends on the nature of the cell envelope and varies across bacterial species. Indeed, differences in bactericidal efficacy of various natural and mimetic surfaces towards Gram-negative and Gram-positive bacteria have been widely investigated.<sup>4,25–29</sup> Surface topography appears to be the key factor in the mechanism for bactericidal activity of nanotextured surfaces<sup>30</sup>;

<sup>a</sup> Biosciences Division, Argonne National Laboratory, Argonne, IL 60439, USA  
E-mail: laible@anl.gov

<sup>b</sup> Center for Nanoscale Materials, Argonne National Laboratory, Argonne, IL 60439, USA

<sup>c</sup> Materials Science Division, Argonne National Laboratory, Argonne, IL 60439, USA  
<sup>d</sup> Department of Biomedical Engineering, Pennsylvania State University, University Park, PA 16802

Electronic Supplementary Information (ESI) available: See DOI: 10.1039/x0xx00000x

it is independent of the chemical composition of the nanopillars.<sup>29,31</sup> In this line of reasoning, the correlation between the antimicrobial properties of various natural nanoprotusions found on the wings of three different cicada species has been reported recently by studying their interactions with *Pseudomonas (P.) fluorescens* species.<sup>32</sup>

The challenge for the materials community is the design and fabrication of nanopatterned antimicrobial structures that target as broad a spectrum of species as possible or, alternatively, selectively kill specific microorganisms. Therefore, a comprehensive study of the interplay between various bacterial cells and designer nanoprotusions is crucially needed, with the aim of engineering surfaces that display higher antimicrobial activities than natural surfaces. To address these challenges, bSi with a wide range of nanotopographies was fabricated using the RIE technique, and the bactericidal effectiveness of these materials towards diverse bacterial genera [*Escherichia (E.)*, *Pseudomonas*, *Rhodobacter (R.)*, and *Bacillus (B.)*] was investigated. Controlled modification of etching conditions reproducibly altered the features of these rough surfaces (e.g., nanopillar length, tip shape, and spacing) as well as their bactericidal properties. Investigation of the interactions of bacteria with bSi surfaces by scanning electron microscopy (SEM) provided insights into the mechanisms for cell killing. To the best of our knowledge, this is the first report on the controlled tunability of bactericidal properties of bSi as well as the first study showing differences in bSi antimicrobial performance not only towards Gram-positive and Gram-negative species but, also – and possibly more importantly – among organisms from the same group.

## 2. Experimental details

### 2.1 Fabrication of bSi

Silicon wafers (4", p-type boron-doped, <100>, resistivity 10–20  $\Omega\text{-cm}^{-1}$ ,  $525 \pm 25 \mu\text{m}$ , purchased from Silicon Quest International) were etched by RIE technique (Oxford PlasmaLab 100) at temperature of 20 °C. The black silicon-regime was found using the protocol developed by Jansen *et al.*,<sup>17</sup> with certain adaptations. Prior to the beginning of the process, wafers were cleaned with acetone. Resulting black silicon fabrication conditions were: RF 100 W, pressure 35 mTorr, back cooling electrode He 5 Torr, O<sub>2</sub> and SF<sub>6</sub> flows 36 sccm (standard cubic centimeter per minute) and 40 sccm, respectively. The etching time was varied between 1.5 and 30 min. The sample used most prevalently (as a benchmark) was prepared by etching for 15 min. To facilitate tests with 1 cm<sup>2</sup> materials samples, full-size wafers were spin-coated with a MEGAPOSIT™ SPR™ 220-7.0 positive photoresist (Rohm and Haas Electronic Materials, LLC), 35 s at 3500 rpm, and baked for 2 min at 115 °C. The wafers were diced into 1 cm<sup>2</sup> pieces and stored for use in future experiments. The photoresist was removed by three times acetone/sonication bath for 2 min.

### 2.2 Characterization of bSi surface

Scanning electron microscopy (SEM) was performed using a JEOL 7500 Field Emission Scanning Electron Microscope, operating at 10–15 kV. The ImageJ program<sup>33</sup> was used in order to determine the mean spike densities based on top views through analysis of at least five independent fields. The spike lengths and base diameters were determined using edge cross sections by counting at least 100 spikes in a given field of the SEM images. The pitch was determined using a nearest-neighbor-distances (NND) ImageJ plugin (<https://icme.hpc.msstate.edu> Author: Yuxiong Mao). Wenzel roughness was determined as shown in *ESI* (Eq. S1–2).

Static water contact angles were determined using a dedicated, contact-angle-measurement device (FM40 *EasyDrop*, KRÜSS GmbH, Hamburg, Germany). Here, 5- $\mu\text{l}$  droplets of deionized water were placed into three different positions on the sample surfaces, and the angles of drops were determined and averaged.

### 2.3 Cell cultures

Three Gram-negative genera *Escherichia*, *Pseudomonas*, *Rhodobacter* and Gram-positive *Bacillus* were used in this study (Table S1). *E. coli* strain DH5 $\alpha$  harboring broad-host-range plasmid pBBR1MCS-2<sup>34</sup> and *B. subtilis* (NCBI 3610) were cultured on LB medium, aerobically, at 37 °C. Aeration of the culture was provided by shaking at 250 rpm. *P. fluorescens* (SBW25) was grown on LB medium at 28 °C and 225 rpm. *R. sphaeroides* and *R. capsulatus* ( $\Delta\text{rshI}[\text{pBBRRWsLsM}]$ )<sup>35</sup> and U43[pBBR1MCS-2], respectively were cultured on <sup>6</sup>YCC (YCC medium<sup>36</sup> containing an additional 1 g/L of yeast extract, pH 7.1) and <sup>5</sup>RCVPY<sup>37</sup> medium, respectively. They were grown under semi-aerobic, chemoheterotrophic conditions in the dark (125 rpm, silicone sponge closures, 33 °C). When appropriate, gentamicin (24  $\mu\text{g/ml}$ ) and kanamycin (30  $\mu\text{g/ml}$ ) were added to the culture medium.

### 2.4 Bacterial cells viability test

**2.4.1 Colony counting method.** The bactericidal activity of bSi was quantitatively evaluated using a plate counting method. Small interaction volumes were utilized to maximize cell-material interactions and to align with anticipated end uses. Bacteria were cultured in rich media until mid-log phase. The cultures were then diluted into fresh medium to the concentration of  $1.6 \times 10^7$  cfu/ml. Prior to the experiment, both black silicon and control surfaces were autoclaved. A 24-well protein crystallization plate containing a pedestal located centrally in a well (Chryschem, Hampton Research) was used as a humidity-controlled experimental system to prevent evaporation (Figure 2a). To assure even humidity, 1 ml of sterile water was added to each well, the wafer/control was placed on the top of pedestal, 20  $\mu\text{l}$  of cells were added, and the well was sealed with vacuum grease and a glass cover slide (22 mm diameter). All experiments were performed at room temperature (RT,  $25 \pm 0.5$  °C) up to 4 h. At given time intervals, cells (20  $\mu\text{l}$ ) were retrieved after *in situ* dilution 1:2 with fresh medium, and serially diluted further to obtain 50–300 colonies per plate with controls. Cell suspensions were plated on rich medium containing appropriate antibiotics as necessary.

Finally, colonies were counted, and bactericidal efficiency was determined based on the percentage of bacteria recovered from bSi *versus* control surfaces.

The controls were chosen experimentally by comparison of growth kinetics of *E. coli* on the various surfaces to their growth in static microfuge tubes (evaluated by OD<sub>600</sub> measurements). The experiments were carried out in the same manner as the viability tests (*vide supra*). The tested control surfaces were non-etched silicon wafers and glass cover slides, and their hydroxylated variants generated by air-plasma exposure for 5 min (for details, see Fig. S1). Glass cover slides were chosen as routine controls as bacterial growth on these surfaces was found invariant to air plasma treatment and increases in culture density matched the growth in culture tubes (measurement of optical densities; OD<sub>600</sub>).

**2.4.2 Live-dead staining and confocal imaging.** The viability of various bacterial species on the bSi substrata was also evaluated by confocal microscopy. The experiments were performed to validate tests based on the plate-counting method. Similar methods were used but with higher concentration of cells for better visualization. Bacteria were grown to mid-log phase and subsequently diluted to  $2.8 \times 10^7$  cfu/ml. At given time intervals, the surfaces were washed three times with 1x TBS to remove planktonic (non-attached) cells as well as traces of medium, followed by staining with LIVE/DEAD<sup>®</sup> BacLight<sup>™</sup> Bacterial Viability Kit (L7012, Invitrogen) per instructions. The kit contains SYTO 9 (green) and propidium iodide (PI, red) dyes that stain the cells depending on their membrane integrity. Bacterial cells with intact membranes are stained green, whereas cells with a damaged membrane (that are considered to be dead or dying) are stained red. Image acquisition and analysis were performed using a Nikon Eclipse Ti microscope with 100x objective, a 1.45 oil immersion lens and NIS-Elements AR 4.50.00 software. The cells were visualized by using 470 and 555 nm excitations and RGB multi-bandpass emission filter. Two color channels, green and red, were acquired for each image. To remove the fluorescent background noise from the image, brightness levels in every channel were adjusted.

### 2.5 SEM imaging of cell/surface interactions

Cells were allowed to interact with the bSi surface for 2 h, washed twice with 1 x PBS, and subsequently fixed using 2.5% glutaraldehyde (GA) solution in 1 x PBS for 30 min ( $V = 50 \mu\text{l}$ ; RT; GA stock 25% in H<sub>2</sub>O). After fixation, surfaces were washed twice in 1 x PBS and subsequently dehydrated in an ethanol series of 25%, 50%, 75%, 95% and 100% (v/v) for 10 min each. Samples were critical point-dried (CO<sub>2</sub>/EtOH), sputter-coated with Au and imaged using a JEOL 7500 Field Emission SEM.

### 2.6 Tracking cell/surface interactions

A fluorescent strain of *B. subtilis* (DK400)<sup>38</sup> was grown in Terrific Broth medium in the presence of IPTG (100  $\mu\text{M}$ ; Sigma Aldrich) at 30 °C for approximately 14-16 hours. A  $\sim 10 \mu\text{L}$  droplet of bacterial suspension (OD<sub>600</sub>  $\sim 2$ ) was transferred to either a bSi (3.6  $\mu\text{m}$  nanopillars) or a smooth, control surface. To minimize evaporation, the 1 cm<sup>2</sup> wafer was enclosed in a sealed, optically clear chamber (of 1.5 cm x 1.5 cm x 0.2 cm dimensions). To observe bacterial motility and interaction of the cells with the silicon surfaces, an inverted microscope Olympus IX71 (10X objective, NA 0.40) and a monochrome camera Prosilica GT1660 were used. Excitation and emission through monochromators was at 587 and 610 nm, respectively. A frame rate of 15 fps (66 ms exposures) was found to be the optimum data acquisition speed that balances fluorescent sensitivity, accurate tracking of bacterial motion, and reduced photobleaching of GFP-containing bacteria. These conditions allowed for acceptable signal-to-noise ratios during experiments that lasted 20-30 seconds. The visual analyses of bacterial dynamics during the initial bSi interaction period allowed detection of distinct events, e.g., sudden stopping and dislodging of the cell by the external shear flow. The sequence of frames was processed in MATLAB using a custom script. While the position of an individual bacterium was tracked manually, the orientation was detected automatically based on a fast Fourier transformation of the bacterium and its surroundings in the image.

## 3. Results and discussion

### 3.1 Fabrication and nanotopography of black silicon

Black silicon fabrication was carried out using the RIE technique as a self-masking process (lithography-free) in  $O_2$  and  $SF_6$  atmosphere where a continuous competition between the etching fluorine radicals and the side-wall-passivating oxygen radicals occurs.<sup>14</sup> To study systematically the impact of bSi topographical features on its antimicrobial performance, a

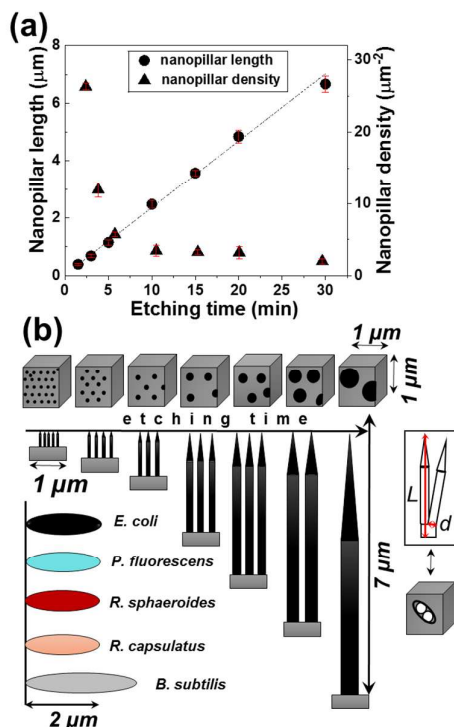


Fig. 1 (a) The temporal evolution of nanopillar morphology (length and density) during the black silicon fabrication process spanning 1.5 to 30 min, and (b) schematic representation of resulting nanostructures. The etching rate is ca.  $220 \text{ nm} \cdot \text{min}^{-1}$ . The observed increase in nanopillar length over time is presented as a cross view (main), and the corresponding nanopillar densities with scale-conserved base diameters as a top view on the surface of  $1 \mu\text{m}^2$  (top). Total pillar length ( $L$ ) is a sum of core plus tip ( $L_{\text{tip}}$ ). In the inset (right), a visualization of twin-pillars sharing a common base is shown, demonstrating how length and base diameter were measured in these cases. Note: when the etching time increases, the presence of these irregular structures also increases contributing to slight underestimation of pillar density at times  $> 20$  min. Relevant sizes of the bacterial cells used for viability experiments are depicted (left; for details, see Table S1).

Table 1 Topographical features of black silicon fabricated for various etching times. The values are presented as a mean  $\pm$  standard deviation. Total length, tip length, base diameter, and pitch were measured for at least 50 pillars by analyzing at least five fields of view. Nanopillar density was measured by analyzing at least five fields of view.

Etching time	Total length	Tip length	Tip angle	Base diameter	Nanopillar density	Pitch	Wenzel roughness
$t$ (min)	$L$ ( $\mu\text{m}$ )	$L_{\text{tip}}$ ( $\mu\text{m}$ )	$\alpha$ ( $^\circ$ )	$d$ (nm)	( $\mu\text{m}^{-2}$ )	(nm)	( $n/a$ )
1.5	$0.39 \pm 0.03$	$0.07 \pm 0.02$	44	$50 \pm 10$	$26.3 \pm 0.4$	$130 \pm 40$	1.79
3	$0.68 \pm 0.05$	$0.12 \pm 0.02$	33	$70 \pm 20$	$11.9 \pm 0.9$	$180 \pm 60$	1.90
5	$1.15 \pm 0.09$	$0.25 \pm 0.05$	23	$100 \pm 10$	$5.7 \pm 0.3$	$280 \pm 90$	1.97
10	$2.48 \pm 0.15$	$0.68 \pm 0.10$	14	$170 \pm 50$	$3.4 \pm 0.8$	$400 \pm 120$	3.17
15	$3.58 \pm 0.10$	$0.81 \pm 0.29$	16	$220 \pm 40$	$3.3 \pm 0.2$	$380 \pm 130$	4.89
20	$4.85 \pm 0.22$	$1.06 \pm 0.40$	17	$320 \pm 80$	$3.1 \pm 0.8$	$490 \pm 130$	8.32
30	$6.67 \pm 0.28$	$2.64 \pm 0.56$	10	$490 \pm 90$	$1.9 \pm 0.3$	$600 \pm 190$	10.74

series of substrates exhibiting various nanotopologies was obtained by modulating etching processes. Through a survey of RIE parameters, we focused here on a related series of topographies that were generated using controlled, reproducible methods with simple changes in etching time, taking advantage of bSi formation dynamics.

The morphology (total nanopillar lengths and densities) of substrates changed dramatically as etching time was increased from 1.5 to 30 min (Fig. 1; for details, see Table 1). A linear correlation between etching time and nanopillar length was found (Fig. 1a, Pearson correlation coefficient 0.9990;  $p < 0.05$ ). An etching rate of  $\sim 3.7 \text{ nm} \cdot \text{s}^{-1}$  ( $\sim 220 \text{ nm} \cdot \text{min}^{-1}$ ) is observed. The nanopillars are 0.4–6.7  $\mu\text{m}$  long and exhibit narrow distributions of lengths (Fig. S2). Correspondingly, there is a marked decrease in nanopillar density (number of pillars per surface area) for the structures. The shortest nanopillars have a density of  $26 \times 10^8 \text{ cm}^{-2}$  and average pitch (center-to-center distance) of 130 nm. At 10 min of etching and beyond, the density reaches a plateau of  $\sim 3 \times 10^8 \text{ cm}^{-2}$  with average pitch  $\sim 420 \text{ nm}$  with distributions that broaden. The frequency of nanopillars on all of the surfaces studied allows for single cells to interact with multiple nanopillars (Fig. 1b), but the possibility for multiple interactions per cell is higher for surfaces etched for shorter times.

A photograph of a full-size bSi wafer reveals the black surface resulting from the layer of nanopillars that present a graded transition of the refractive index from air to the bulk Si layer (Fig. 2a).<sup>12,19</sup> It is noteworthy that very slight variations in the gas ratio affected the homogeneity of the surface structure, with striking impacts upon spike shape and density (narrow slot in gas ratio phase space for bSi; data not shown).<sup>17</sup>

Why is the density decreasing? At the beginning of the process, many nucleated pillars are present. During the course of etching, smaller and thinner needles become shadowed by larger pillars and are constantly eliminated leading to the observed decrease in their density as well as a shift in the average pitch towards greater distances (Fig. S5). These nanotopological features are in general agreement with

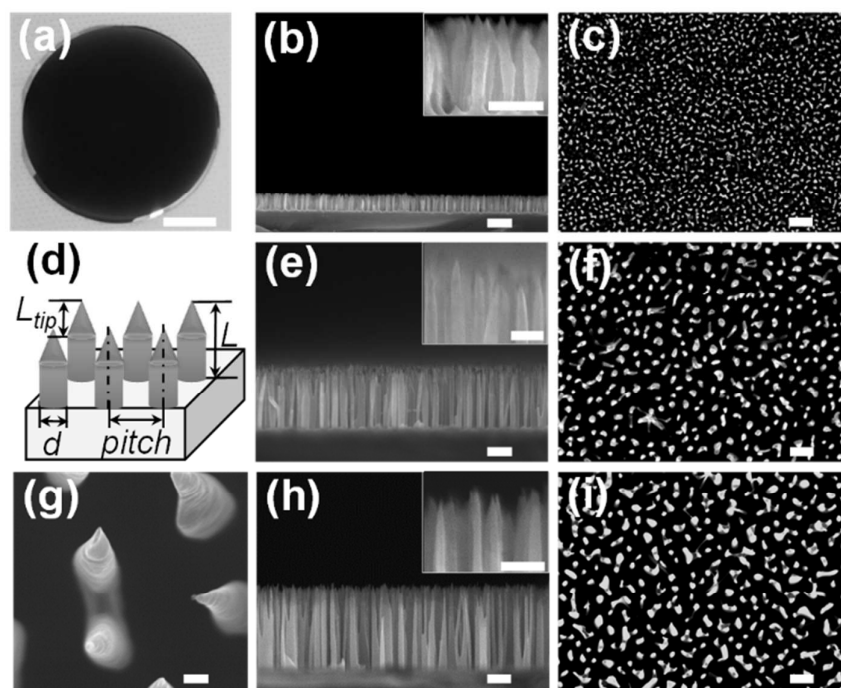


Fig. 2 Topographical features of black silicon. (a) A photograph of the etched 4" wafer after 15 min plasma exposure. (b, c, e-i) SEM micrographs presenting the nanotopography of black silicon fabricated using a range of etching times: (b-c) 3 min, (e-f) 10 min, and (g-i) 15 min. (b, e, h) Cross sections with insets presenting a magnified view of the pillars (b) or the top portions of the pillars (tips; e, h), and (c, f, g, i) top views of etched surfaces. (d) A schematic representation of the pillars where  $L$  is total length,  $L_{tip}$  is a length of sharpened tip,  $d$  is base diameter, and pitch is a distance between centers of two pillars (spacing + diameter). Scale bars are conserved at  $1\ \mu\text{m}$  in all images, except (a) 2.5 cm, and (g) 100 nm, and insets of (b, e, h) 400 nm.

The morphological and structural properties of bSi were investigated by means of SEM. Figure 2b-i shows micrographs of representative nanopillar architectures of bSi for selective etching times, as well as a schematic representation of the resulting bSi morphologies, illustrating quantitation procedures and important features such as total nanopillar length, tip length, base diameter and pitch (Fig. 2d) that are modified by extended etching of the surface. The images clearly reveal that longer etching time not only results in an increase in nanopillar length but also in a decline in nanopillar density (see top views, from 11 to 3 pillars per  $1\ \mu\text{m}^2$  for 3 and 15 min etching, respectively, and Fig. S3). The sharpness of the nanopillars is also enhanced by longer etching with tip angles decreasing from  $44^\circ$  to  $10^\circ$  (Table 1; Fig. S4).

studies performed by Pezoldt *et al.*<sup>39</sup> Additionally, as the etching time increases, the base diameter also widens and the frequency of the occurrence of multiple (double or triple) pillars originating from a common base increases.

Importantly, tip geometry also changes. Although pillars possess relatively sharp tips after 3 min of plasma exposure, some of them exhibit an onion-like structure with a shorter tip and a "bulb" (Fig. 2b, inset). Similar bulbous morphologies of bSi tips have been reported by Pham *et al.* for pillars of an analogous length of  $\sim 620\ \text{nm}$ .<sup>40</sup> After 10 and 15 min of etching, the pillar tips become more uniform and very sharp (Fig. 2g, and insets of Fig. 2e and 2h).

### 3.2 Surface wettability

The antimicrobial activities of surfaces of varied wettability have been studied intensively as this parameter affects bacterial adhesion<sup>41–44</sup>. As such, surface wettabilities for this series of bSi etchings were characterized with static water contact angle (CA) measurements. Starting materials were moderately hydrophilic with CAs averaging  $\sim 40^\circ$ , but all etched substrata became superhydrophilic (rough surfaces of materials, on which water spreads completely with a CA of  $\sim 0^\circ$ )<sup>45</sup>, except the surface of the shortest nanopillars of 390 nm where the CA was  $\sim 20^\circ$ . We note that these surface characteristics as well as morphologies were not altered once exposed to heat and high pressure (autoclave; allowing for a means of surface sterilization, *vide infra*).

The bactericidal efficiencies (BE, determined based on the percentage of bacteria recovered from bSi *versus* control surfaces, see Eq. S3) of the various surfaces were surveyed initially using *E. coli* as a model Gram-negative species. While bacteria continued to grow on the control surfaces over time, a significantly reduced number of cells was found with the bSi surfaces (Fig. 3b–c, Fig. S7).

Here, three characteristic regimes (Fig. 3c, 4 h) of topographies were identified that exhibit similar bactericidal behavior: blunt and short pillars (I), pillars of intermediate features (II), and sharp and long pillars (III). The antibacterial activity was lowest for surfaces with the shortest nanopillars (regime I) that most closely mimic the dimensions of the waxy protrusions found in

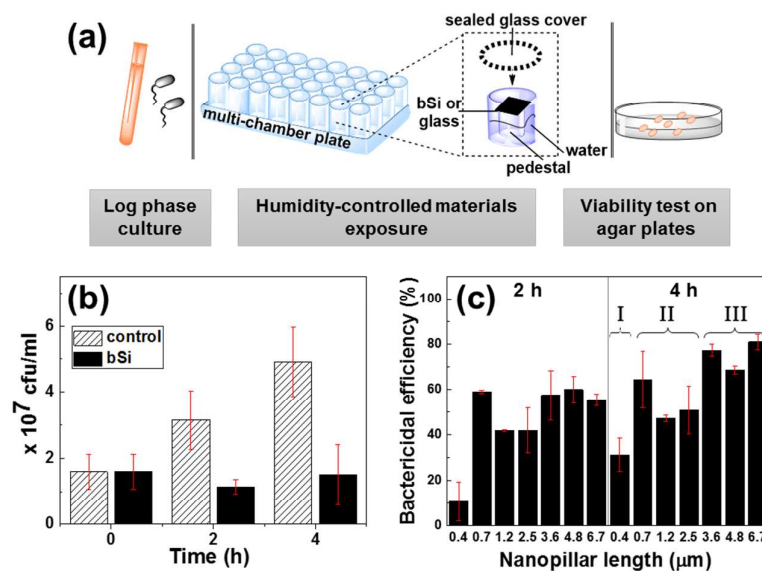


Fig. 3 Bacterial viability on black silicon surfaces. (a) Schematic of experimental workflow. (b) Bactericidal effect of bSi ( $L = 3.6 \mu\text{m}$ ) on *E. coli* in rich medium at room temperature. Whereas cell multiply on a smooth surface, cell killing or growth inhibition is observed on nanostructured surfaces. (c) Bactericidal efficiencies of bSi of various topographies towards *E. coli*. All the values are expressed as a mean  $\pm$  SD ( $n = 3$  independent experiments).

Based on Wenzel and Cassie-Baxter models (Fig. S6a) describing CA of rough surfaces, the measured CA can be explained as a combination of the CA of the starting material and the roughness factor (defined by Wenzel as a ratio of the areas of the etched and the smooth surface). To promote complete liquid spreading on a surface of given intrinsic CA, a minimum roughness value is required.<sup>45</sup> For this set of surfaces, it appears that a dimensionless roughness value of  $\sim 1.9$  is the point that renders a surface superhydrophilic; this was not quite fulfilled in the case of the sample plasma-etched for 1.5 min, possessing roughness of 1.8 (Table 1).

### 3.3 Bactericidal performance *versus* various topographies

Bactericidal properties of the fabricated surfaces were studied by depositing droplets of cell suspensions in rich medium on top of bSi [Fig. S6b; and on a smooth, non-etched control surface], incubating, plating retrieved cells, and comparing the number of colonies that appeared. These bactericidal experiments were performed in humidity-controlled microchambers (Fig. 3a). For convenience, the various bSi topographies are referred to by nanopillar lengths.

nature (with the possible exception that these surfaces exhibit a wider distribution in pillar shapes and densities; Fig. S8). A previously published report suggested that bactericidal activity of the nanotextured surfaces increases when number of pillars interacting with bacteria also increases.<sup>32</sup> Departing from this observation, we found that the bSi surface with the highest nanopillar density showed the lowest BE values for *E. coli*. Indeed, in the regime II, BEs were found to be pillar density-dependent. Within this short-to-mid nanopillar range ( $L = 0.7 \mu\text{m} - 2.5 \mu\text{m}$ ), where the nanopillar density decreases dramatically from *ca.* 12 pillars to *ca.* 3 pillars per  $\mu\text{m}^2$ , bactericidal performance at early time (2 h) were 59%, 42%, and 42%, respectively. This density dependence continues to hold at longer surface-interaction times (4 h).

The dependence on density is lost for surfaces with nanopillars longer than  $3 \mu\text{m}$  when BEs are the highest observed (range between 69–81 % after 4 h of incubation). The longest needles outperformed the shortest ones by over a factor of two. Although these different BE values may have many origins, it is apparent that sharpness of the nanopillars dramatically

improves with the etching time and, thus, with nanopillar length.

### 3.4 Topographies versus various bacterial species

The impact of representative surfaces from the three bactericidal regimes (I - 0.4, II - 0.7 and III - 3.6  $\mu\text{m}$ ) on the bactericidal efficiency of various bacterial species was investigated (Fig. 4a-b). Strains from an additional three genera – *Pseudomonas*, *Rhodobacter*, and *Bacillus* – were

rigidity is a combination of glycan chains that are cross-linked with peptides and proteins that connect peptidoglycan with an outer membrane. Glycan chains are generally considered the least flexible of the components<sup>46</sup>. Although it is assumed that peptidoglycan organization is similar in most of the Gram-negative bacteria, in each species the cell wall contains a set of unique proteins that reflect the adaptation to a specific ecological niche.<sup>47</sup> Additionally, it has been suggested that the character of bonding between the peptidoglycan and the outer membrane (covalent vs. electrostatic) contributes to overall

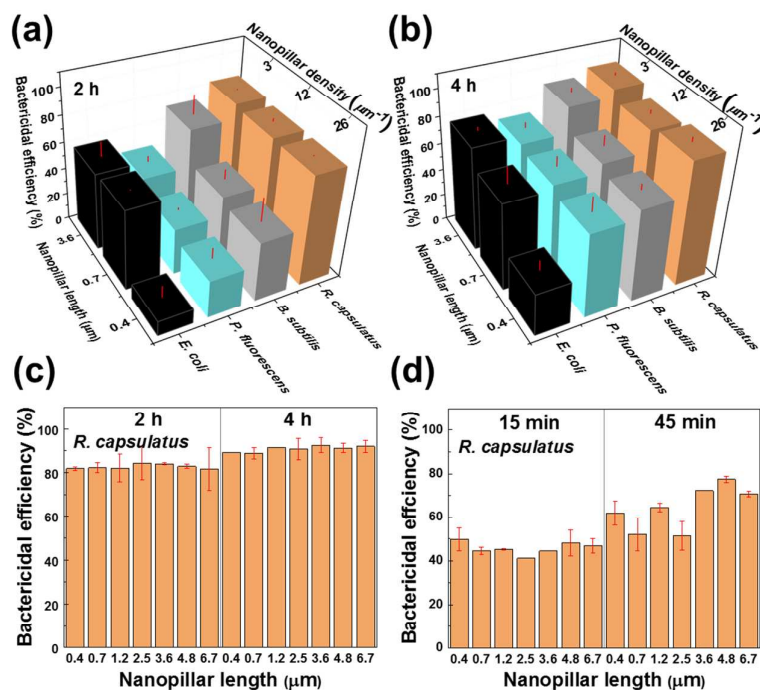


Fig. 4 Bactericidal efficiencies of black silicon of three nanopillar lengths towards four genera with (a) 2 h and (b) 4 h incubations. (c-d) *R. capsulatus* for an expanded set of bSi surfaces (seven in total). Bacteria were incubated in rich medium at room temperature on black silicon and smooth control surfaces for (c) 2 and 4 h, and (d) for 15 and 45 min. The values are presented as a % of control and are expressed as a mean  $\pm$  SD ( $n = 3$  independent experiments).

chosen as they (along with *E. coli*) represent model laboratory species from biomedical, soil and aquatic environments. After 2 h incubation (Fig. 4a), interestingly, *R. capsulatus* showed an extreme sensitivity to bSi independent of the topography (average killing across all surfaces of 83%). In contrast, *E. coli*, *P. fluorescens*, and *B. subtilis* were killed less efficiently than *R. capsulatus*. The dependence on bSi topography was shown to be the strongest for *E. coli*, intermediate for *P. fluorescens* and *B. subtilis*, and the weakest for *R. capsulatus*. This pattern holds for longer incubation times (Fig. 4b).

In this study, we focused on responses of various Gram-negative species and compared them to results obtained for a Gram-positive representative *Bacillus*. Surprisingly, *B. subtilis* cells, which have a much thicker peptidoglycan layer than Gram-negative cells, was killed with higher efficiencies than *E. coli* and *P. fluorescens*, suggesting that peptidoglycan layer thickness is likely not the only factor in observed differences between species (Fig. 4).<sup>4,29</sup>

The differences between the Gram-negative species may be attributed to dissimilarities in their cell-wall stiffness. This

cell rigidity.<sup>22,48</sup>

To gain insight into the apparent lack of effect of bSi surface-topography on *R. capsulatus* killing (Fig. 4c-d), a wider range of seven bSi surfaces with nanopillar lengths extending up to 6.7  $\mu\text{m}$  was used. The BE values were constant for all bSi surfaces studied when experiments were conducted for 2 or 4 h. A weak but significant surface-dependent killing could be observed only after 45 min incubation, consistent with a higher BE for longer and sharper nanopillars (Fig. 4d). Approximately half of *R. capsulatus* cells were dead after only a 15 min exposure to bSi surfaces, indicating that the killing kinetics for this species were nearly an order of magnitude faster than for *E. coli*. The killing process continued over time, yielding nearly quantitative killing of *Rhodobacter* after 45 min of interaction with surfaces containing pillars greater than 3  $\mu\text{m}$ . These BE values were comparable with those found after 2 h of incubation.

Attributes of the strains of bacteria tested (Table S1) were compared to the geometries of the bSi nanopillars (Fig. 1b). For all species examined, bactericidal activities of longer

nanopillars at lower densities appear to be enhanced by the distinctly greater sharpness and tip length of nanopillars. The lengths of these nanopillars were approximately 10-20 times greater than the lengths of bactericidal protrusions found in nature (typically ~150-440 nm) or bSi reported previously (~620 nm).<sup>26,32,40</sup> BE values markedly increased to range from ~71 to 98% (for details, see Fig. S9). These observations are supported by theoretical studies that indicate that antimicrobial properties of nanopatterned surfaces are enhanced when pillars are sharper and the distance between the adjacent pillars increases.<sup>49</sup>

staining allows characterization of cells present or remaining on the surface and can distinguish viable from dead cells, whereas the colony-counting technique only indicates the viability of planktonic cells (that may or may not have interacted with the surface) and those which were able to detach from the surface during washing steps and recover. The methods are complementary and are required in order to fully characterize antimicrobial properties of surfaces.

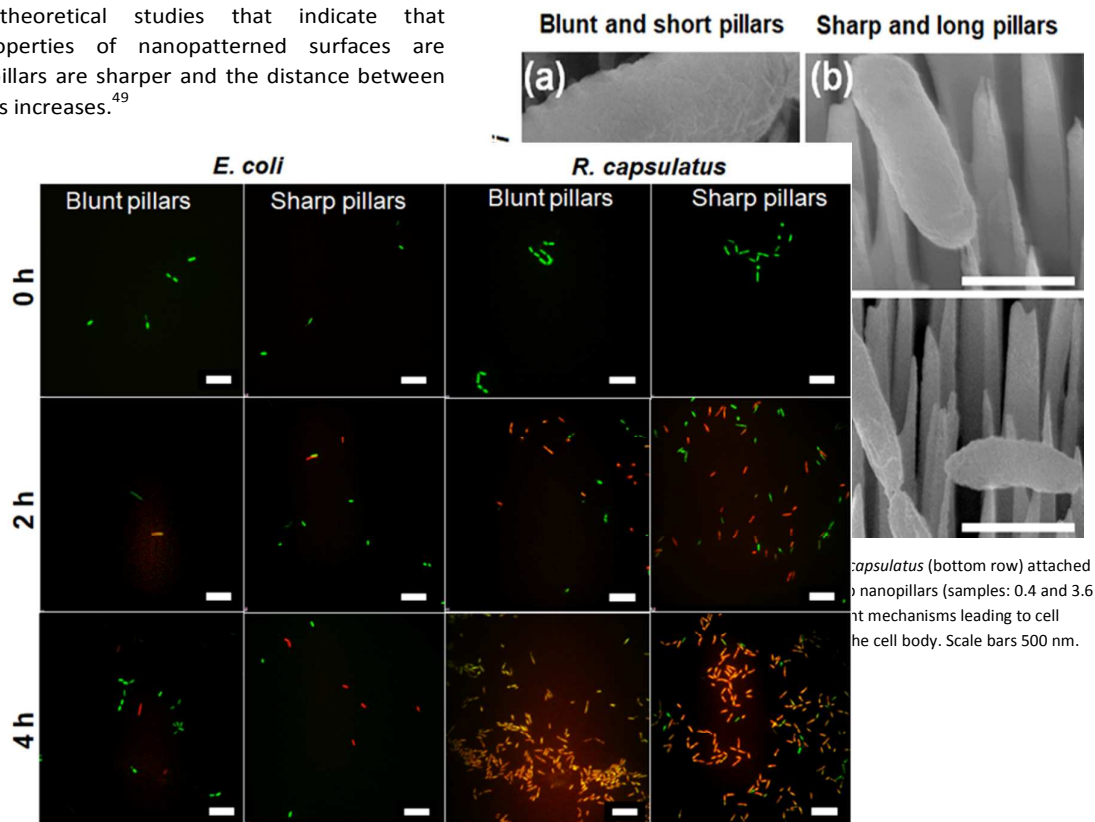


Fig. 5 Confocal microscopy images of *E. coli* and *R. capsulatus* attached to the surface of bSi at 0, 2 and 4 h of incubation. Two surfaces were tested: 0.4 and 3.6  $\mu\text{m}$  that correspond to blunt and sharp nanopillars. Cells were stained with a bacterial viability kit where green and red dyes label live and dead cells, respectively. Scale bar 10  $\mu\text{m}$ .

The contribution to killing of clustered pillars (commonly two or three) emerging from a common base (e.g., Fig. 1b) – the frequency of which increases concomitantly (broad pitch distributions at long times; Fig. S5) – is not currently understood. These clusters provide numerous “islands” of heterogeneity where spike pitch/density is locally increased, rendering it possible for a single bacterial cell to be impaled by multiple, exceedingly sharp nanopillars. These clusters likely entrap and rupture cells rapidly and irreversibly.

### 3.5 Microscopic validation

The colony-counting method revealed distinct differences in the interactions of *E. coli* and *R. capsulatus* with 0.4 and 3.6  $\mu\text{m}$  nanopillars (designated as short/blunt and long/sharp, respectively, hereafter). Confocal microscopy was used to examine the nature of the event(s) that led to the reduction in the number of viable cells to determine whether its origins were enhanced adhesion or actual killing events. Live/ dead

The images presented in Fig. 5 reveal that the majority of both *E. coli* and *R. capsulatus* cells attached on the bSi surface were dead after 4 h in case of sharp nanopillars (see Fig. S10 for *P. fluorescens* and *B. subtilis*). On the blunt surface, dead *E. coli* cells were scarce, but the frequency of dead *R. capsulatus* cells was as high as on the sharp nanopillars. The results confirm plate-based counts. We also noticed that *Rhodobacter* showed much larger numbers of surface-attached cells relative to the other bacteria. These results are corroborated by higher adhesion of *R. sphaeroides* (a related species) to hydrophilic mica surfaces relative to *E. coli*.<sup>50</sup>

Also, adhesion of dividing cells to nanostructures might interfere with cell elongation, mid-cell division, and/or separation of the daughter cells. One or both cells may be disrupted or become detached from the surface. The rapid growth rates of *E. coli* and *P. fluorescens* may allow one sister cell to escape from the material surface as the other sister is being killed.<sup>27</sup>

### 3.6 New mechanistic insights

The most commonly reported mechanism describing bSi-mediated cell death is associated with tip-enhanced penetration of bacterial cell walls.<sup>4</sup> In contrast, it has been suggested that nanopillars displaying spherical caps (blunt; more resembling those found in nature) act by rupturing the membrane of a cell that is suspended between adjacent pillars; this action results from stretching forces rather than direct impalement<sup>23</sup>. In order to gain more mechanistic insights into the bactericidal activity of bSi, SEM imaging was used to examine cell-pillar interactions (Fig. 6-8). Indeed, sharp pillars clearly pierce the cells (Fig. 6b,d) whereas blunt pillars do not (Fig. 6a,c). Except for the dissimilarity in killing efficiencies for short pillars found by colony-counting and live/dead staining methods, no obvious distinctions in cell-pillar interactions were found between species.

As shown for *E. coli* (Fig. 7), the mechanism of death is a process of adhesion to nanopillars (a,d), followed by stretching of the membrane (blunt, b) or piercing (sharp, e), provoking cytoplasm leakage and complete cell rupture (c,f). Eventually, the cell body either rests atop blunt nanopillars (c), never

reaching the bulk Si, or hangs from the sharp tips that pierced them (f). In some cases, sharp pillars can be seen to pass through both sides of the cell (Fig. S11). The tips of blunt pillars were never observed to stick up through the cellular debris/deflated cells as for the sharp pillars, further indicating that the mechanism of killing for these nanopillars is not direct piercing. Both mechanisms could be working in the case of pillars of intermediate length.

Although bSi topography is a major factor in the bactericidal mechanism, our findings also demonstrate that killing strongly depends on cellular features that enhance interactions with the bSi surface. The attractive strength (bacterial adhesion) towards the surface is known to play a role and it leads to membrane stretching.<sup>51</sup> Especially in the case of the mechanism for short, blunt nanopillars, this step seems to be particularly important. In general, adhesion is driven by multiple factors including surface chemistry, environment, and properties of the bacterial cell wall that include structural features such as the presence and cellular distribution of flagella and fimbriae, and the chemical composition of lipopolysaccharides.<sup>52,53</sup>

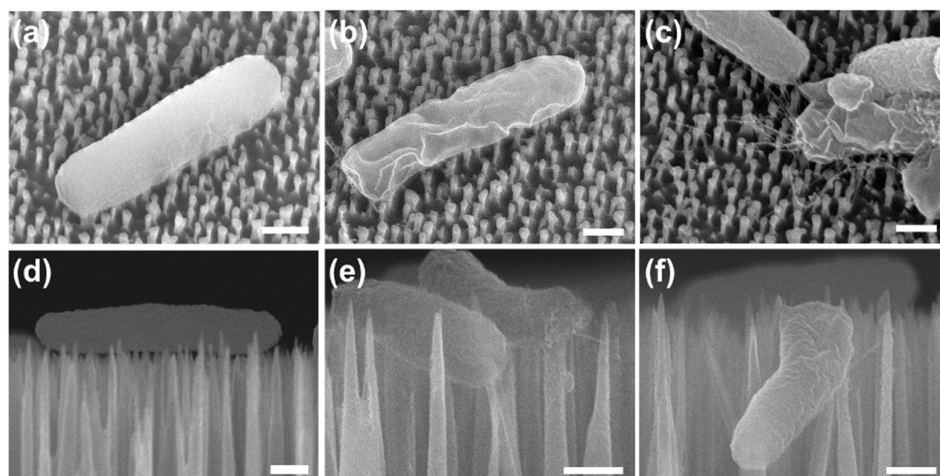


Fig. 7 SEM images of *E. coli* at various stages of interactions with black silicon surfaces: (a-c) blunt and (d-f) sharp nanopillars (samples: 0.4 and 3.6  $\mu\text{m}$ , respectively). Scale bars 500 nm. In order to visualize both cell and materials features in the same image, specimens are tilted 30° (a-c) or 90° (d-f).

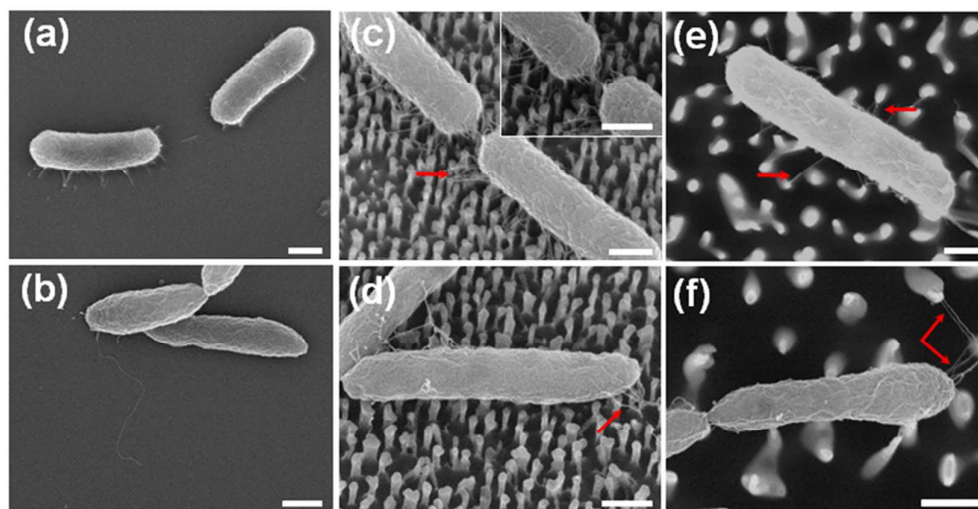


Fig. 8 SEM micrographs of *E. coli* (top row) and *R. capsulatus* (bottom row) attached onto smooth (a-b) and black silicon surfaces: (c-d) blunt and (e-f) sharp nanopyllars (samples: 0.4 and 3.6  $\mu\text{m}$ , respectively). The red arrows indicate bacterial adhesins arranged around nanofeatures. Scale bars 500 nm. (a-d) tilted 30°, (e-f) top views.

Figure 8 shows the arrangement of these appendages around nanofeatures (red arrows), indicating their role when interacting with such surfaces. These outward-facing and dynamic cellular features affect the ability of cells to interact with surfaces through a variety of means (e.g., electrostatic interactions, van der Waals forces, hydrophobic interactions, and hydrogen bonding).<sup>42</sup> However, no study thus far has demonstrated the impact of various surface chemistries on the bactericidal performance of the material.<sup>8</sup> The controlled synthesis of bSi of varied nanotopographies may be used in the future to distinguish between the impacts of some of these biotic/abiotic interactions and may result in the design of experiments to better determine mechanisms of cell death induced by natural as well as synthetic nanotextured materials.

It is noteworthy that although long and sharp pillars always exhibit the best antimicrobial performance, there are some differences in bactericidal rate between species (Fig. 4). Rapid death of *Rhodobacter* species suggests that cell penetration by sharp pillars occurs nearly immediately after these cells associate with bSi tips. However, similar BE in the case of *E. coli* was found to require at least 2 h. Thus, differences in cellular rigidity between bacterial species may come into play. The results may also indicate that *E. coli* requires a longer time of interaction on the tips to generate the tension and stretching that is sufficient for disruption of this cell type. After all, they are ultimately pierced (Fig. 6-8). Tension imparted by a single nanopyllar or cluster of nanopyllars is a direct result of tip geometry and their compatibility with the cell-wall and cytoskeletal-like structures of these bacterial species. Inspiration for how these cellular parameters lead to differences in the species-dependent BE observed may be derived from mechanisms that have recently been used with success to describe nanowire penetration of eukaryotic cells of various stiffness.<sup>51</sup>

Additional mechanistic insights may be revealed using fluorescently labelled strains that allow visualization of the interactions of cells with these surfaces in real time, a technique that has been absent from this field thus far. Cells dynamically interacting with etched and smooth surfaces are captured in Supplementary Videos 1 and 2. Motility tracking was used to distinguish between reversible and permanent attachments (Fig. S12). Based on cellular velocities and angles between the cells and their direction of motion, *B. subtilis* cells are killed within just a few seconds of interacting with sharp nanopyllars. Time-lapse confocal imaging will be an important tool for these studies moving forward as they lead to a mechanistic understanding of bactericidal activity of nanotextured surfaces. Here, 2D or 3D bacterial tracking<sup>54</sup> will be used (i) to differentiate between a set of proposed mechanisms and (ii) to identify key cellular properties that allow for selectivity of bactericidal effects.

#### 4. Conclusions

Protection from bacterial infection and colonization is afforded in biology by nanotexturing on the surfaces of plants, insect wings, lizards, and sharks. Many synthetic analogs have emerged with similar antimicrobial activities. We present, for the first time, advances in materials fabrication that have generated performance-enhanced mimetics with antimicrobial activities that are shown to be superior to those of natural surfaces (either exceptional killing percentages and rates or selectivity in species that were targeted). The characterization of these surfaces and bactericidal activities was approached systematically and allowed us to identify key material parameters that affect the way in which bacteria interact with these surfaces and eventually lead to cell death. The characterization of the activity of these surfaces was accentuated by time-lapse confocal microscopy that captured

events that are indicative of cellular immobilization and rupture. Two different mechanisms are obvious in the interaction of microbial cells with these textured surfaces. The longer, exceedingly sharp pillars are capable of piercing all types of microbial cells directly and are found to be nonselective regarding species. The shorter, blunt pillars require multifaceted cellular interactions that eventually stretch and tear the membrane envelopes. These interactions appear to be species specific and result in differential rates of interaction and disruption.

The properties of the nanotexturing appear to dictate the mechanism by which the surface interacts with and disrupts the cell. We find that the rate of killing by a selected surface is dictated by the properties of the bacterial cell (e.g., nature of the cell wall, peptidoglycan layer, and outer membrane; abundance and localization of flagella; extent and composition of secreted polysaccharides, etc.). Additional studies of more diverse members of the bacterial kingdom will likely reveal correlations that can be used for designer materials that specifically target or avoid select classes or species of microbes. Once properly tuned for an application, these advanced surfaces can be deployed as antimicrobial agents in ways that are just beginning to be envisioned: from display on biomedical, food preparation, and water purification surfaces to incorporation into cosmetics or use as enhancements in agrochemical pesticides.

## Conflicts of interest

The authors declare no conflict of interest.

## Acknowledgements

The authors thank Deborah Hanson, Marie-Françoise Gros, Gasper Kokot and Claire Kohout for discussions. This material is based upon work supported by Laboratory Directed Research and Development (LDRD) funding from Argonne National Laboratory, provided by the Director, Office of Science, of the U.S. Department of Energy under Contract No. DE-AC02-06CH11357. Use of the Center for Nanoscale Materials, an Office of Science user facility, was supported by the U. S. Department of Energy, Office of Science, Basic Energy Sciences, under the same contract.

## References

- 1 J. Min, K. Y. Choi, E. C. Dreaden, R. F. Padera, R. D. Braatz, M. Spector and P. T. Hammond, *ACS Nano*, 2016, **10**, 4441–4450.
- 2 H. Chen, M. Zhang, B. Li, D. Chen, X. Dong, Y. Wang and Y. Gu, *Biomaterials*, 2015, **53**, 532–544.
- 3 A. Elbourne, R. J. Crawford and E. P. Ivanova, *J. Colloid Interface Sci.*, 2017, **508**, 603–616.
- 4 E. P. Ivanova, J. Hasan, H. K. Webb, G. Gervinskias, S. Juodkakis, V. K. Truong, A. H. F. Wu, R. N. Lamb, V. A. Baulin, G. S. Watson, J. A. Watson, D. E. Mainwaring and R. J. Crawford, *Nat. Commun.*, 2013, **4**, 2838.

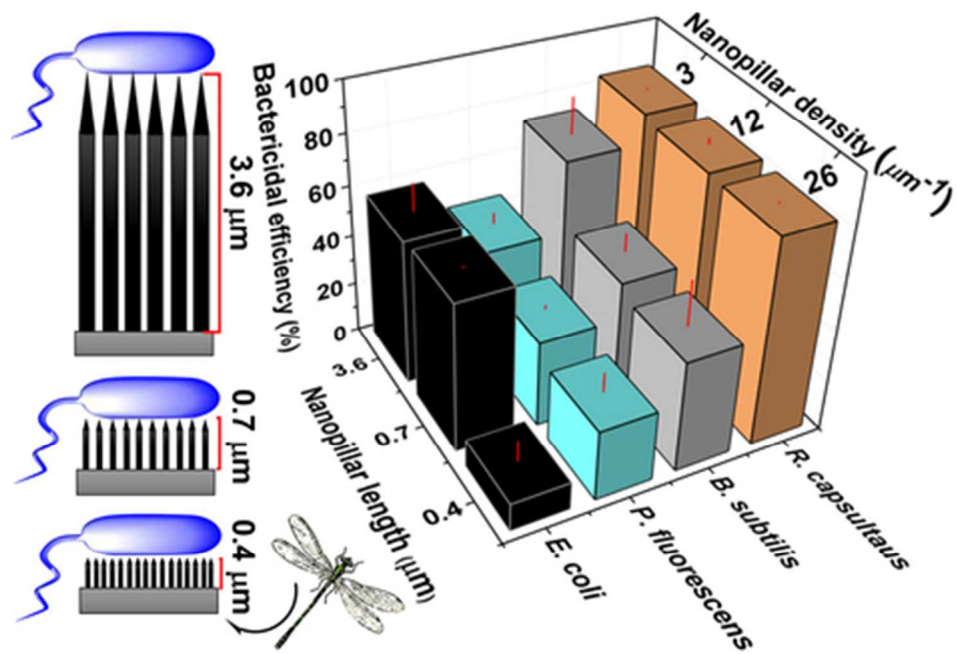
- 5 C. M. Bhadra, V. K. Truong, V. T. H. Pham, M. Al Kobaisi, G. Seniutinas, J. Y. Wang, S. Juodkakis, R. J. Crawford and E. P. Ivanova, *Sci. Rep.*, 2015, **5**, 16817.
- 6 T. Sjöström, A. H. Nobbs and B. Su, *Mater. Lett.*, 2016, **167**, 22–26.
- 7 M. N. Dickson, E. I. Liang, L. A. Rodriguez, N. Vollereaux and A. F. Yee, *Biointerphases*, 2015, **10**, 21010.
- 8 A. Susarrey-Arce, I. Sorzabal-Bellido, A. Oknianska, F. McBride, A. J. Beckett, J. G. E. Gardeniens, R. Raval, R. M. Tiggelaar and Y. A. Diaz Fernandez, *J. Mater. Chem. B*, 2016, **4**, 3104–3112.
- 9 S. H. Nguyen, H. K. Webb, P. J. Mahon, R. J. Crawford and E. P. Ivanova, *Molecules*, 2014, **19**, 13614–13630.
- 10 J. O. Lee, V. Narasimhan, J. Du, B. Ndjamien, D. Sretavan and H. Choo, *Adv. Healthc. Mater.*, 2017, **6**, 1601356.
- 11 V. T. H. Pham, V. K. Truong, A. Orłowska, S. Ghanaati, M. Barbeck, P. Booms, A. J. Fulcher, C. M. Bhadra, R. Buividas, V. Baulin, C. J. Kirkpatrick, P. Doran, D. E. Mainwaring, S. Juodkakis, R. J. Crawford and E. P. Ivanova, *ACS Appl. Mater. Interfaces*, 2016, **8**, 22025–22031.
- 12 Y. Lu and A. R. Barron, *ACS Appl. Mater. Interfaces*, 2015, **7**, 11802–11814.
- 13 H. V. Jansen, M. J. de Boer, S. Unnikrishnan, M. C. Louwse and M. C. Elwenspoek, *J. Micromechanics Microengineering*, 2009, **19**, 33001.
- 14 X. Liu, P. R. Coxon, M. Peters, B. Hoex, J. M. Cole and D. J. Fray, *Energy Environ. Sci.*, 2014, **7**, 3223–3263.
- 15 E. Axente, M. Sopronyi, C. Matei Ghimbeu, C. Nita, A. Airoudj, G. Schrodj and F. Sima, *Carbon N. Y.*, 2017, **122**, 484–495.
- 16 A. V. Singh, *J. Biomed. Mater. Res. Part A*, 2013, **101**, 2994–3008.
- 17 H. Jansen, M. de Boer, R. Legtenberg and M. Elwenspoek, *J. Micromechanics Microengineering*, 1995, **5**, 115–120.
- 18 J. Gao, M. de Raad, B. P. Bowen, R. N. Zuckermann and T. R. Northen, *Anal. Chem.*, 2016, **88**, 1625–1630.
- 19 L. Sainiemi, V. Jokinen, A. Shah, M. Shpak, S. Aura, P. Suvanto and S. Franssila, *Adv. Mater.*, 2011, **23**, 122–126.
- 20 M. Steglich, T. Käsebier, M. Zilk, T. Pertsch, E.-B. Kley and A. Tünnermann, *J. Appl. Phys.*, 2014, **116**, 173503.
- 21 M. S. Schmidt, A. Boisen and J. Hubner, in *2009 IEEE Sensors, IEEE*, 2009, pp. 1763–1767.
- 22 R. D. Turner, W. Vollmer and S. J. Foster, *Mol. Microbiol.*, 2014, **91**, 862–874.
- 23 S. Pogodin, J. Hasan, V. A. Baulin, H. K. Webb, V. K. Truong, T. H. Phong Nguyen, V. Boshkovikj, C. J. Fluke, G. S. Watson, J. A. Watson, R. J. Crawford and E. P. Ivanova, *Biophys. J.*, 2013, **104**, 835–840.
- 24 C. D. Bandara, S. Singh, I. O. Afara, A. Wolff, T. Tesfamichael, K. Ostrikov and A. Oloyede, *ACS Appl. Mater. Interfaces*, 2017, **9**, 6746–6760.
- 25 J. Hasan, H. K. Webb, V. K. Truong, S. Pogodin, V. A. Baulin, G. S. Watson, J. A. Watson, R. J. Crawford and E. P. Ivanova, *Appl. Microbiol. Biotechnol.*, 2013, **97**, 9257–9262.
- 26 V. K. Truong, N. M. Geeganagamage, V. A. Baulin, J. Vongsvivut, M. J. Tobin, P. Luque, R. J. Crawford and E. P. Ivanova, *Appl. Microbiol. Biotechnol.*, 2017, **101**, 4683–4690.
- 27 C. Sengstock, M. Lopian, Y. Motemani, A. Borgmann, C. Khare, P. J. S. Buenconsejo, T. A. Schildhauer, A. Ludwig and M. Köller, *Nanotechnology*, 2014, **25**, 195101.
- 28 J. Hasan, S. Jain and K. Chatterjee, *Sci. Rep.*, 2017, **7**, 41118.
- 29 T. Diu, N. Faruqui, T. Sjöström, B. Lamarre, H. F. Jenkinson, B. Su and M. G. Ryadnov, *Sci. Rep.*, 2014, **4**, 7122.
- 30 A. Tripathy, P. Sen, B. Su and W. H. Briscoe, *Adv. Colloid Interface Sci.*, 2017, **248**, 85–104.
- 31 E. P. Ivanova, J. Hasan, H. K. Webb, V. K. Truong, G. S. Watson, J. A. Watson, V. A. Baulin, S. Pogodin, J. Y. Wang, M. J. Tobin, C. Lobbe and R. J. Crawford, *Small*, 2012, **8**, 2489–2494.
- 32 S. M. Kelleher, O. Habimana, J. Lawler, B. O' Reilly, S. Daniels, E. Casey and A. Cowley, *ACS Appl. Mater. Interfaces*, 2016, **8**, 14966–14974.

## ARTICLE

## Journal Name

- 33 C. a Schneider, W. S. Rasband and K. W. Eliceiri, *Nat. Methods*, 2012, **9**, 671–675.
- 34 M. E. Kovach, P. H. Elzer, D. S. Hill, G. T. Robertson, M. A. Farris, R. M. Roop and K. M. Peterson, *Gene*, 1995, **166**, 175–176.
- 35 N. P. Dylla, K. M. Faries, R. M. Wyllie, A. M. Swenson, D. K. Hanson, D. Holten, C. Kirmaier and P. D. Laible, *FEBS Lett.*, 2016, **590**, 2515–2526.
- 36 A. K. W. Taguchi, J. W. Stocker, R. G. Alden, T. P. Causgrove, J. M. Peloquin, S. G. Boxer and N. W. W. J., 1992, **31**, 10345–10355.
- 37 C. Kirmaier, P. D. Laible, K. Czarnecki, A. N. Hata, D. K. Hanson, D. F. Bocian and D. Holten, *J. Phys. Chem. B*, 2002, **106**, 1799–1808.
- 38 M. M. Genkin, A. Sokolov, O. D. Lavrentovich and I. S. Aranson, *Phys. Rev. X*, 2017, **7**, 11029.
- 39 J. Pezoldt, T. Kups, M. Stubenrauch and M. Fischer, *Phys. status solidi*, 2011, **8**, 1021–1026.
- 40 V. T. H. Pham, V. K. Truong, D. E. Mainwaring, Y. Guo, V. a. Baulin, M. Al Kobaisi, G. Gervinskias, S. Juodkazis, W. R. Zeng, P. P. Doran, R. J. Crawford and E. P. Ivanova, *J. Mater. Chem. B*, 2014, **2**, 2819.
- 41 X. Zhang, L. Wang and E. Levänen, *RSC Adv.*, 2013, **3**, 12003–12020.
- 42 D. Campoccia, L. Montanaro and C. R. Arciola, *Biomaterials*, 2013, **34**, 8533–8554.
- 43 X. Dou, D. Zhang, C. Feng and L. Jiang, *ACS Nano*, 2015, **9**, 10664–10672.
- 44 A. V. Singh, S. Baylan, B.-W. Park, G. Richter and M. Sitti, *PLoS One*, 2017, **12**, e0175428.
- 45 J. Drelich and E. Chibowski, *Langmuir*, 2010, **26**, 18621–18623.
- 46 V. Vadillo-Rodriguez and J. R. Dutcher, *Soft Matter*, 2009, **5**, 5012–5019.
- 47 R. Koebnik, K. P. Locher and P. Van Gelder, *Mol. Microbiol.*, 2000, **37**, 239–253.
- 48 V. Vadillo-Rodríguez and J. R. Dutcher, *Soft Matter*, 2011, **7**, 4101–4110.
- 49 F. Xue, J. Liu, L. Guo, L. Zhang and Q. Li, *J. Theor. Biol.*, 2015, **385**, 1–7.
- 50 Z. Oestreicher, A. Taoka and Y. Fukumori, *Micron*, 2015, **72**, 8–14.
- 51 X. Xie, A. M. Xu, M. R. Angle, N. Tayebi, P. Verma and N. A. Melosh, *Nano Lett.*, 2013, **13**, 6002–6008.
- 52 K. Anselme, P. Davidson, A. M. Popa, M. Giazzon, M. Liley and L. Ploux, *Acta Biomater.*, 2010, **6**, 3824–3846.
- 53 R. S. Friedlander, H. Vlamakis, P. Kim, M. Khan, R. Kolter and J. Aizenberg, *Proc. Natl. Acad. Sci.*, 2013, **110**, 5624–5629.
- 54 K. M. Taute, S. Gude, S. J. Tans and T. S. Shimizu, *Nat. Commun.*, 2015, **6**, 8776.

New forms of hydrophilic black silicon with superior bactericidal properties that can be tailored to selectively kill specific species.



39x27mm (300 x 300 DPI)